Full Length Article

Additive manufacturing assisted investment casting: A low-cost method to fabricate periodic metallic cellular lattices

V.H. Carneiro[a],*, S.D. Rawson[b], H. Puga[c], J. Meireles[a], P.J. Withers[b]

[a] MEtRiCS-Mechanical Engineering and Resource Sustainability Center, Campus of Azurém, 4800-058, Guimarães, Portugal
[b] The Henry Royce Institute, Department of Materials, The University of Manchester, Manchester, M13 9PL, UK
[c] CMEMS-UMinho, University of Minho, Campus of Azurém, 4800-058, Guimarães, Portugal

ARTICLE INFO

ABSTRACT

Metallic cellular solids are a class of materials known for their high specific mechanical properties, being desirable in applications where a combination of high strength or stiffness and low density are important. These lightweight materials are often stochastic and manufactured by foaming or casting. If regular (periodic) lattice structures are desired, they may be manufactured by metallic additive manufacturing techniques. However, these have characteristic issues, such as un-melted powders, porosity and heterogeneous microstructures. This study reports a novel low-cost route for producing regular lattice structures by an additive manufacturing assisted investment casting technique. Fused filament fabrication is used to produce the lattice structure pattern which is infiltrated with plaster. The pattern is then burnt off and the aluminum is cast in vacuum. In this way we can manufacture non-stochastic metallic lattices having fine struts/ribs (0.6 mm cross-section using a 0.4 mm nozzle) and relative densities down to 0.036. X-ray micro computed tomography (μCT) showed that as-cast A356 Aluminium alloy frameworks have high dimensional tolerances and fine detail control. Frameworks based on units of six connected struts ranging from intruding (auxetic) to protruding (hexagonal) strut angles are studied. Vertical struts are finer than expected, reducing their moment of area which could impact their compressive strength. This new, low cost, route for producing high precision metallic cellular lattices offers an attractive alternative to other additive manufacturing techniques (*e.g.* selective laser and electron beam melting).

1. Introduction

Cellular foams are characterized by an interconnected scaffolding network in which stochastic solid cellular structures are surrounded by a fluid phase or gas [1,2]. Due to their low relative density and high specific strength these materials are attractive in transportation (*e.g.* aerospace [3,4], aeronautic [5,6], railway [7–9] and naval [10,11]), medical (*e.g.* prosthesis [12,13] and stenting/scaffolding [14]), among other industries [15,16]. In most applications where load bearing capacity or energy absorption are key, the solid phase is generally metallic in nature [17].

Metallic stochastic cellular materials are typically manufactured by melt infiltration using foaming/blowing agents [18–20], casting with space holders [21–23], powder metallurgy [24,25] or wire weaving [26–28]. However, their stochastic nature makes the control of their relative (to the bulk solid) properties challenging, for example modulus (E^*/E_s) and density (ρ^*/ρ_s) [1,29]. For cellular solids it is usually considered that these two properties are related *via* a power law: $(E^*/E_s) =$ $(\rho^*/\rho_s)^2$ [2,29].

Recently, researchers have found benefits in the development of non-stochastic metallic cellular lattices. Unsurprisingly it has been found that these regular configurations enable better the control of the deformation mechanisms and, thus, allow the precise tailoring of mechanical properties [17,30]. However, their fabrication typically involves more complex manufacturing techniques. There have been significant developments on metallic additive manufacturing (AM) applied to the production of cellular lattices, such as: selective laser sintering/melting (SLS or SLM) [31,32], direct metal laser sintering (DMLS) [33,34] and electron-beam melting (EBM) [35–37].

Even though these techniques are able to produce structures with relatively thin-walls and struts (thicknesses ~0.24 to 0.80 mm [38–40]), they can have significant drawbacks in terms of dimensional and microstructural control [41,42]. Metallic AM parts are known to have macro-scale defects [43–48], such as: (i) un-melted powder (*i.e.* lack of fusion); (ii) circular or tunneled/network porosity; (iii) delamination; and (iv) distortion. At a microstructural scale, such processes

---

* Corresponding author.
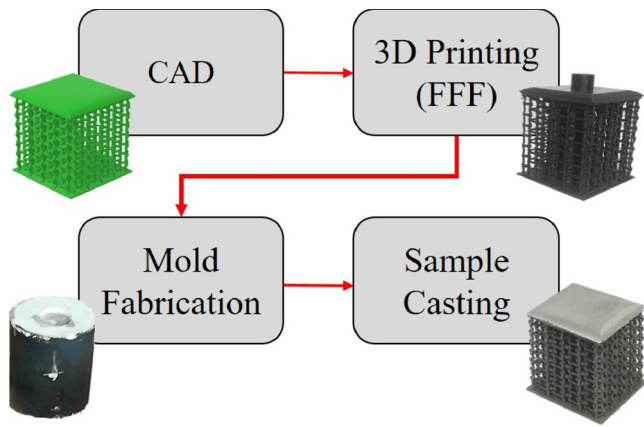 *E-mail address:* d6705@dem.uminho.pt (V.H. Carneiro).

Fig. 1. Flowchart for the proposed additive manufacturing assisted investment casting technique.

are associated with extreme temperature variations in their melting-solidifying cycles [38]. Consequently, they may have grains with different morphologies [40,45,49,50] (*e.g.* lamellar, equiaxed, columnar and dendritic) and anisotropic behavior dependent on the build direction. This heterogeneous microstructure may be further accentuated by cyclic recrystallization during the repeated deposition of layers [44].

Metal casting allows excellent microstructural [51–53] and dimensional control [54,55]. Moreover, there have been significant improvements on the filling of thin-walled structures [56]. Most of the difficulties associated with the casting of cellular lattices arise from mold production issues [57]. Here we circumvent many of these issues by the fabrication of polymeric investment models by AM, and subsequent investment casting to produce fine metallic cellular lattices.

This study presents several geometries of non-stochastic metallic cellular lattice structures manufactured *via* AM polymer investment model fabrication followed by investment casting of A356 aluminium alloy. We have optimized the printing parameters to produce samples with low density by maximizing strut length and minimizing strut cross-section. As-cast samples have been imaged and characterized in 3D using micro computed tomography (μCT) to determine the effect of the manufacturing process on sample dimensions, shapes and defects.

2. Methodology

Fig.1 shows that the proposed technique comprising a combination of 3D-printing and investment casting. An initial (CAD) design of the sample was used as a reference from which to produce the PLA pattern by fused filament fabrication (Fig. 1). This pattern acts as the template for the plaster mold that was filled with the molten aluminum to produce the metallic cellular lattices.

2.1. Lattice geometry

Individual cells (Fig. 2) were based around a 6-sided two dimensional (2D) 'honeycomb' framework, being defined by two horizontal ribs and four oblique struts having a square cross-section. According to the individual unit cell displayed in Fig. 2, the fundamental repeating unit was described in terms of horizontal ribs (h) and oblique (l) strut lengths, thickness (t) and angle (α). In this study, the linear dimensions (h, l and t) were varied to optimize the structural design, while the angle (α) was changed to produce 'honeycomb' cells having different geometries.

The individual cells made up a two-dimensional lattice (Fig. 2(b)), linked by common struts. These lattices were repeated in the three Cartesian axis to produce a three-dimensional (Fig. 2 (c) - 9 × 9 × 8 matrix) lattice. Skins (*i.e.* plates) on the top and bottom faces enclosed the lattice core. The samples were modeled by CAD using SolidWorks 2016 (Dassault Systèmes, Vélizy-Villacoublay, France) (Fig.3).

2.2. 3D-printing the investment casting model

The lattice structure patterns (Fig.3) were 3D-printed in Polylactic acid (PLA) by fused filament fabrication using a BCN3D Sigma printer (BCN3D, Barcelona, Spain). The design of the patterns allowed 3D-printing without requiring support materials, ensuring a simple and fast manufacturing process.

The printing parameters are listed in Table 1. The extrusion/bed temperatures (T) and printing speed (P_s) were in accordance with equipment manufacturer guidelines and kept constant. Nozzle diameters (N) and layer heights (L_h) were optimized to provide a successful print (*i.e.* all details are printed) whilst minimizing printing time. Ten replicates were analyzed for each case. Printing parameters were considered successful if all prints were able to reproduce the full CAD model, considering the XY plane (Fig.2) as the building plane.

2.3. Forming the investment cast

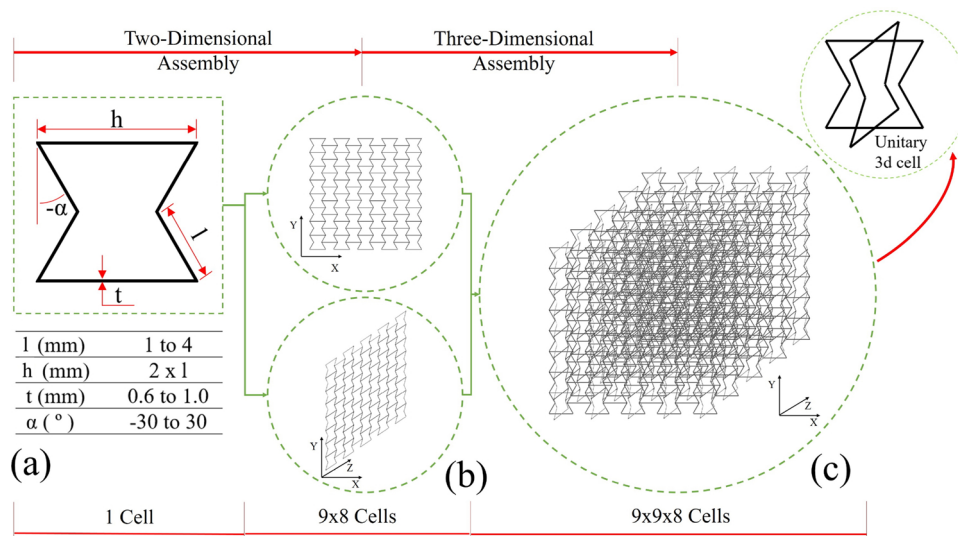The 3D-printed polymer patterns were subsequently infiltrated with

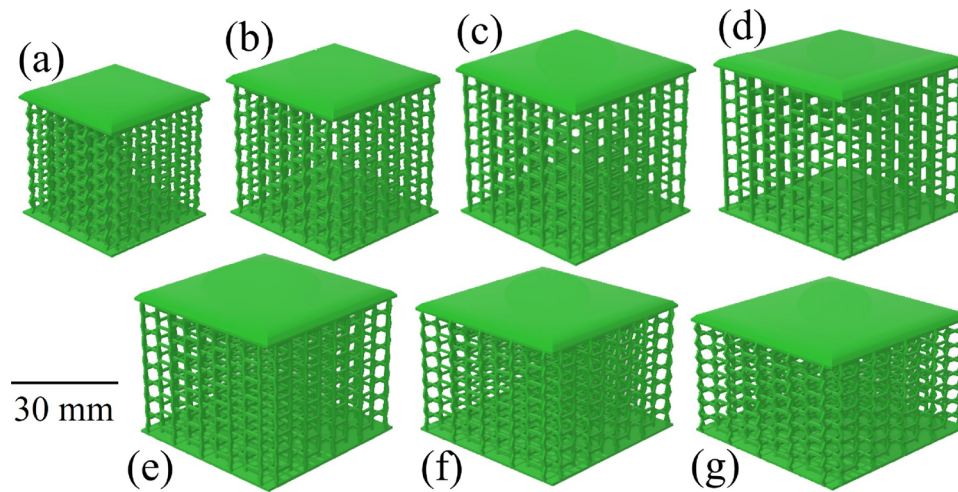**Fig. 2.** Lattice design process: (a) 2D unit cell; (b) 2D and (c) 3D lattice.

l (mm)	1 to 4
h (mm)	2 x l
t (mm)	0.6 to 1.0
α (°)	-30 to 30

Fig. 3. CAD models representations of samples with: (a) α = -30°, (b) α = -20°, (c) α = -10°, (d) α = 0°, (e) α = 10°, (f) α = 20° and (g) α = 30°.

Table 1
3D-printing (fused filament fabrication) parameters.

Material		Polylactic Acid (PLA)
N - Nozzle diameter (mm)		0.3; 0.4; 0.6; 1
L_h - Layer height (mm)		0.05; 0.10; 0.15; 0.20; 0.30; 0.40
P_s - Printing speed (mm/s)		10
T – Temperature (ºC)	Extrusion	210
	Bed	40

liquid plaster (30 %$_m$ distilled water and 70 %$_m$ GoldStar Omega + plaster, Staffordshire, UK) to produce ceramic molds. The molds were then subjected to the thermal cycle represented in Fig.4. The polymer patterns were completely eliminated during this thermal treatment.

This thermal cycle allowed the plaster to cure completely, while ensuring high precision for the investment model shape and dimensions. During the first stage of the curing cycle (isothermal at 300 °C for 3 h) the PLA model began to evaporate. At the end of the second stage (ramp from 300 °C to 730 °C in 5 h), only trace residues of the PLA model was found (~0.12 %$_{wt}$). Thus, during the third and fourth stages (respectively, isothermal at 730 °C for 6 h and cooling to 250 °C), the

PLA pattern was eliminated and all details were embossed in the ceramic mold.

2.4. Casting the metallic cellular lattice

A356 Al alloy (24 g) was cut from a primary fusion ingot (Fig. 5 (a)). After being cleaned and dried using compressed air, the alloy was inserted in a SiC crucible, along with Al5Ti1B (0.05 g – 0.2 %$_{wt}$) and Al10Sr (0.07 g – 0.3 %$_{wt}$) master alloys to promote grain refinement and eutectic Si modification. The maximum material for the lattice was 21 g, corresponding to 87.5 % of total crucible capacity. The remaining 3 g (12.5 % crucible capacity) corresponded to the casting gating system thereby assuring sufficient metalo-static pressure during the liquid metal filling.

The alloy was melted (700 °C) inside an Indutherm MC15+ (Indutherm, Walzbachtal, Germany) induction casting furnace. The melt was kept isothermal at 700 ± 2 °C for 3 min for homogenization, while the imposed induction magnetic stirring prevented nucleant particle sedimentation. After this period, the melt was cast (Fig. 5 (b)) in vacuum (P = -1 bar) into the pre-heated ceramic mold (250 ± 5 °C). Following a 10 min solidification period, the ceramic mold was submerged in water to separate the plaster from the cast samples.
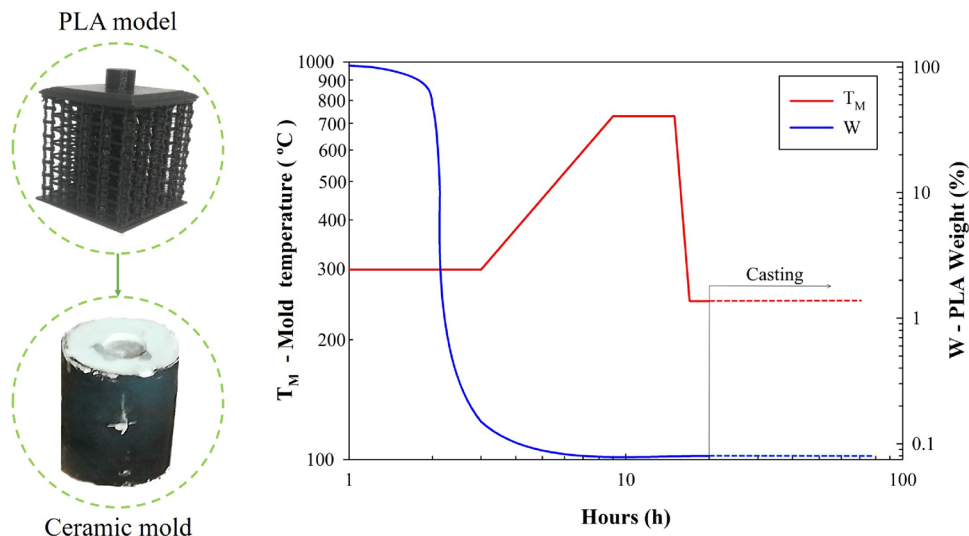

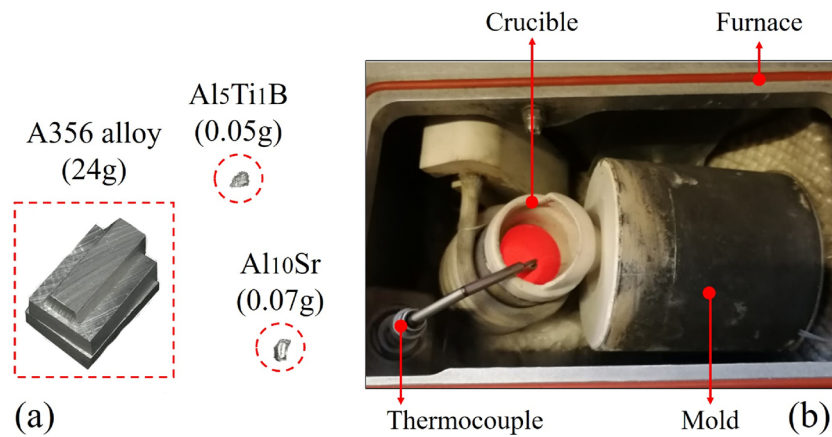**Fig. 4.** Thermal cycle and PLA weight during ceramic mold fabrication.

Fig. 5. Casting process: (a) A356 and Al5Ti1B/Al10Sr alloys being (b) cast into the mold (furnace top view).

Table 2
X-ray CT parameters.

Sample	$-30°$	$-20°$	$-10°$	$0°$	$10°$	$20°$	$30°$
Voxel size (µm)	20.9	26.5	26.5	26.5	27.2	56.7	56.7
Exposure time (s)	4	4	4	4	1	1	1
Source-sample distance (mm)	130	165	190	192	192	192	192
Sample - detector distance (mm)	80	45	45	45	36	36	36
No. of projections	2401	3001	3001	3001	3001	3001	3001

2.5. Dimensional characterization by X-ray micro computed tomography

X-ray micro computed tomography (µCT) imaging was performed using a Zeiss Versa XRM-520 µCT scanner (Zeiss, Oberkochen, Germany) controlled using the XRM scout-and-scan control system (v.1.1.5707.17179; Zeiss, Oberkochen, Germany). Samples were mounted on a polystyrene wedge to minimize cone-beam artefacts (one sample of each geometry was imaged). All scans were performed using a 0.39x objective lens and LE3 filter, with a voltage of 140 kV and power of 10 W and projections were taken through 360° of rotation. The remaining imaging settings were optimized for each sample and are summarized in Table 2.

Data was reconstructed using XRM reconstruction software (Zeiss, Oberkochen, Germany), then segmentation and visualization was performed using Avizo standard (version 9.0 Visualisation Sciences Group, Oregon, USA). Cross-sections through the reconstructed 3D volume were exported as 2D tiff image stacks to allow measurement of the strut dimensions. The overall dimensions of the samples and the struts were measured from the micrographs using Fiji [58]. Statistical analysis was performed on the sample rib and strut measurements. Data was checked against the normal distribution (found to be not normal) and then significant differences were calculated using a one-way ANOVA on Ranks (Kruskal-Wallis test – for significance of $p < 0.05$ and $p < 0.01$).

3. Results and discussion

3.1. Analysis of the 3D printed PLA pattern

The printing parameters played a prominent role in determining the overall shape of the patterns. Fig. 6 represents the ability of the 3D-printer to produce these patterns using different nozzles. Smaller nozzle diameters were able to produce ribs and struts with lower thickness values, which is desirable to minimize specific density. It should be noted that strut thicknesses less than 0.6 mm could not be produced

with the nozzles employed.

These printing failures occurred due to under-extrusion of the printing filament (*e.g.* Fig. 7 (a)), caused by the wear of the filament in the extrusion gear (Fig. 7 (b)). Filament wear was caused by the change in velocity in the extrusion/retraction cycles needed to deploy reduced amounts of PLA in each individual strut [59]. In conclusion, the minimum strut cross-section that was achieved was 0.6 mm, using nozzle diameters lower than 0.4 mm.

Printing success was also dependent on the layer heights (L_h) of each printing layer, according to the results in Table 3. As layer height was increased, the printing eventually failed due to the lack of adherence. Our results demonstrated that whilst increasing layer height reduced printing time, the layer height should not exceed 0.2 mm to assure sufficient printing adherence. The 0.4 mm nozzle, alongside a layer height of 0.2 mm, was therefore selected to minimize the printing time without compromising printing success.

3.2. X-ray computed tomography of metallic cellular lattices

Fig. 8 shows examples of the final as-cast samples in which the details may be observed and compared with the CAD models (Fig.3). It is apparent that casting was able to faithfully reproduce the intended shape and details.

µCT imaging was performed of the cast samples (Fig.9) allowing a detailed inspection of the samples, including the internal configuration of each individual periodic cell.

Measurement of µCT volume data (Fig.10 (a)) demonstrates that the as-cast sample height (H_S) was higher (by approximately +0.2 to +0.4 mm (~0.75 to 1.50 %)) than the CAD model. The strut angle influenced the dimensional variations in the widths and depths (W_S and D_S - Fig. 10 (b)) of the cast samples. Negative/positive strut angles produced negative/positive width and breadth dimensional variations (-0.54 mm to 0.26 mm, respectively, -1.60 % to 0.26 %) respectively. According to Fig.10 (c), these dimensional variations affected the relative density (ρ^*/ρ_0), with frameworks having negative angles slightly higher than expected (Fig. 10(c).

Fig. 11 shows examples of the periodic cellular units found in the cast cellular lattices. Samples with negative angles (Fig. 11 (a) to (c)) had a honeycomb configuration comprising intruding struts. This morphology is characteristic of cellular lattices having negative Poisson's ratios (*i.e.* auxetic behavior) [60]. Fig. 11 (d) had a square-shaped cell ($\alpha = 0°$), where the rib and struts were essentially horizontally and vertically configured. The samples with positive strut angles (Fig. 11 (e)–(g)) had a classic honeycomb (*i.e.* hexagonal) configuration with a positive Poisson's ratio [17].

Fig. 12 shows that the strut angle had an impact on the overall shape of the cell and on the ability of the manufacturing process to
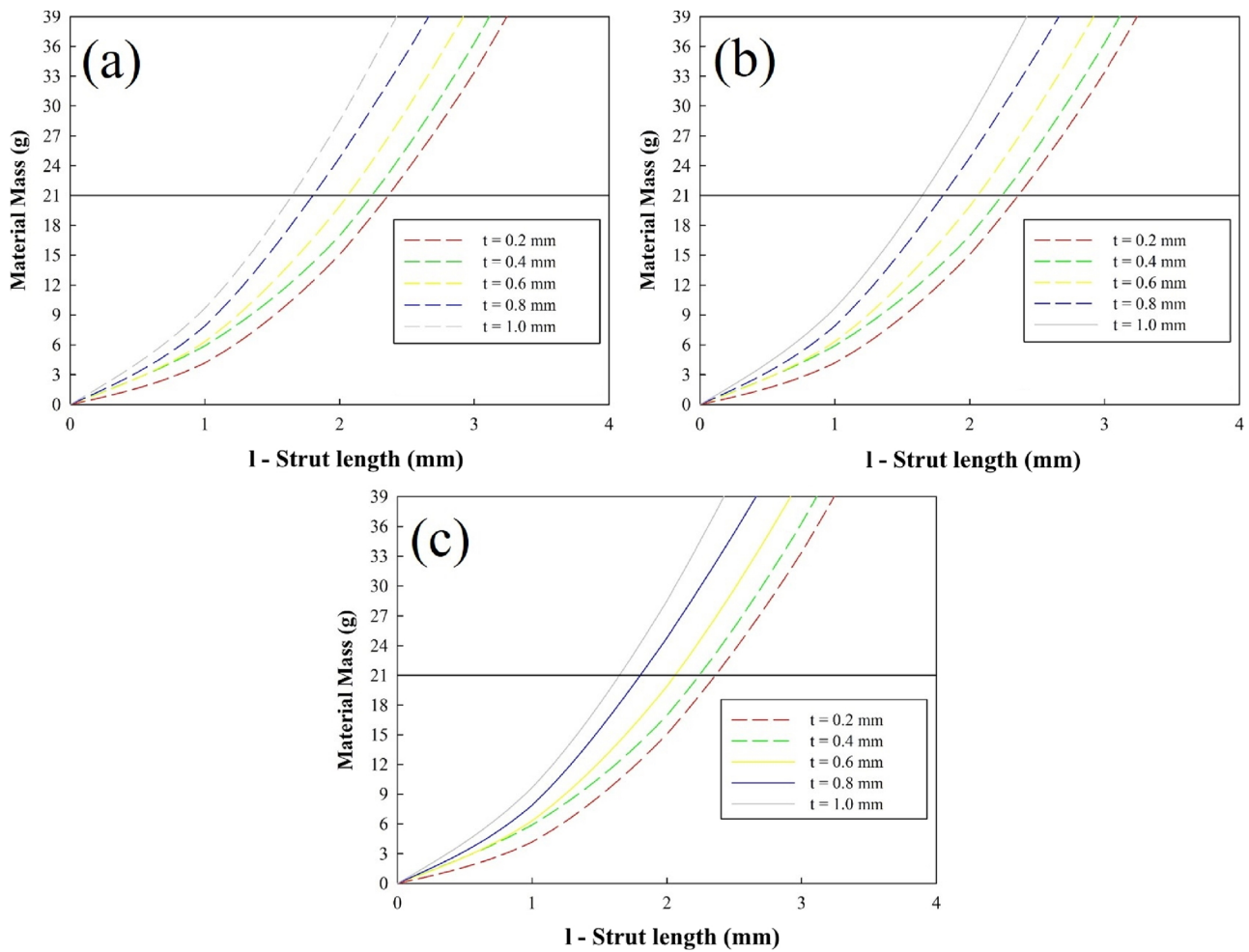
Fig. 6. Relationship between strut thickness (t) (defined in the CAD model) and required alloy material mass, for nozzle diameters of: (a) 1 mm, (b) 0.6 mm, (c) 0.4 and 0.3 mm ($\alpha = 30°$, $P_s = 5$ mm/s and $L_h = 0.05$ mm in all cases). Note: horizontal lines denote crucible limit; Dashed lines denote printing failure.
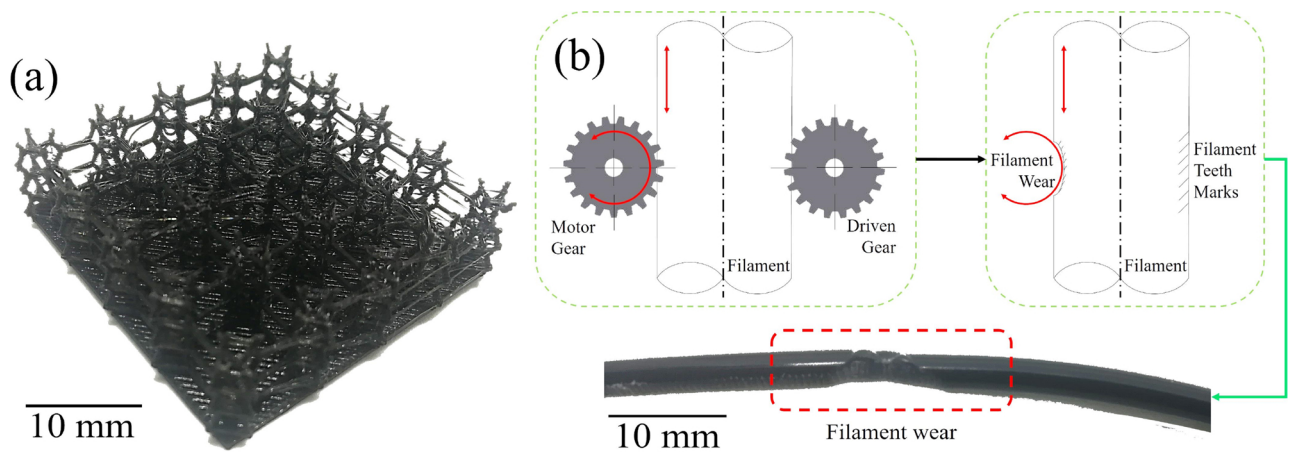

Fig. 7. Printing failure: (a) whole sample failure by (b) under-extrusion due to filament wear ($\alpha = 30°$, $P_s = 5$ mm/s, $L_h = 0.05$ mm and N = 0.3 mm).

faithfully replicate the CAD design. The true strut angles (α_{TRUE}) displayed an angular error (from -1.40° to 0.73°, see Fig. 12 (a)). These errors were relatively small in comparison with the deviations in the linear dimensions (h, l, and t).

Fig. 12 (b) and (c), show that the variation in the median horizontal rib (h) and strut (l) lengths, which had more pronounced dimensional variations. This indicated a more prominent role in the overall dimensional variations of the cast samples (Fig. 10). Horizontal ribs

(Fig. 12 (b)) and struts (Fig. 12 (c)) had a dimensional range of -0.50 % to 3.75 % and 0.04%–10%, respectively. Such changes were more prominent in samples having wider angles, either negative or positive. We hypothesize this to be attributed to the different bending stiffness of the struts during the printing process.

It is known that during 3D-printing, thin inclined struts (*e.g.* $\alpha = -30°$ or $\alpha = 30°$) are subjected to: (i) bending due to contact between the strut and the rigid nozzle [61,62]; and (ii) coalescence between PLA in

Table 3

Relation between nozzle diameter, layer height, printing time and the successful printing of the models (t = 0.6 mm and v = 2 mm; n = 10 replicates).

Printing time		N – Nozzle diameter (mm)	
		0.3	0.4
L_h	0.05	6.5 hours	5.5 hours
Layer	0.10	3.5 hours	3.0 hours
height	0.15	2.5 hours	2.0 hours
(mm)	0.20	2.0 hours	1.75 hours
	0.30	-	-
	0.40	-	-

	Successful printing
	Printing failure

the nozzle and layers by higher surface tension [63]. Further, the more inclined struts (*e.g.* $\alpha = -30°$ or $\alpha = 30°$) are subjected to bending while the nozzle extrudes material, whereas struts that are essentially vertically aligned ($\alpha \sim 0°$) are more prone to axial loads [62].

Although strut cross section (t) (Fig. 12 (d)) had relatively little impact on the exterior cast sample dimensions (Fig. 10 (a) and (b)), it did affect the sample density (Fig. 10 (c)). In broad terms there was a tendency for the samples to have finer struts than the CAD models. This was more noticeable when the strut angle was approximately zero ($\alpha \sim 0°$, Fig. 12 (d)). Such a change in the geometry of the cross-section also affected on the strut cross-sectional area.

The strut dimensions displayed in Fig. 12 were subjected to non-parametric statistical testing to analyze their significance (Table 4), where the X-ray μCT measurements were compared. In terms of angular dimensions (α_{TRUE}– Fig. 12 (a)), given that each sampling group was supposed to display different strut angles, significant differences between them were expected. Table 4 shows that there was a clear difference between the groups, although when comparing samples with $\alpha = 0°$ and $\alpha = 10°$, this difference was less significant ($p < 0.05$) than the other possible combinations ($p < 0.01$).

When the different groups were compared in terms of strut and rib lengths (h and l; Table 4), apart from the wider strut angles ($\alpha = -30°$ and $\alpha = 30°$) the different groups were not significantly different.

The statistical analysis of strut thickness (t) did not seem to follow a

clear trend. In fact, according to Table 4, most groups showed a significant difference with each other. This may have been attributed to the overall variations in the 3D-printing process of the PLA investment model. Given that the layer height was constant ($L_h = 0.2$ mm), struts with wider angles (Fig. 13 (a)) had fewer layers than samples with lower strut angles (Fig. 13 (b)). Since the 3D-printing process followed the sample Cartesian planes, the layer deposition in inclined struts occurred in a tilted cross-section (*e.g.* Fig. 12 (a)), generally referred to as a staircase [64] surface. These changes, however, were not applicable to the printing process of the horizontal ribs (Fig. 13 (c)) in which the printing area was more elevated and constant. All these factors generated significant statistical differences in strut thickness.

For struts, the printing area (P_A - Fig. 13 (d)) of each layer varied with the strut angle according to $P_A = (t^2)/\cos(\alpha)$. Due to the discrete segmentation process during the G-code programming, this also occurs in metal-based AM [65]. It is known that there is a deterioration of strut geometry at inclined angles relative to the build platform [47,65,66]. However, in metal AM techniques this issue is mainly attributed to the dissipation of heat flux through the neighboring sintering powder in oblique struts [67].

Given that the equipment positioning resolution in the XX and YY axes was 12.5 μm [68], the reduction in printing area for the near-zero strut angle ($\alpha \sim 0°$) effectively reduced the strut printing area (Figs. 12 (d) and 13 (c)). Due to the equipment resolution and the circular shape of the nozzle, the resultant investment model exhibited a quasi-circular cross-section instead of the square cross-section prescribed by the CAD (Fig. 14).

Since extrusion could not be stopped instantly, the constant movement of the extrusion head and filament introduced viscoelastic effects [69], the nozzle introduced protrusion defects in some areas, as observed in the μCT volume images (Figs. 11 and 15).

Fig. 16 (a) shows a reduction in the strut area, especially for near-zero strut angles ($\alpha \sim 0°$), as demonstrated by the model in Figs. 13 and 14. Furthermore, this changed their strut moment of area through: (i) the reduction in strut thickness (t – Fig.12 (d)); and (ii) change in cross-section from a square ($I_\blacksquare = t^4/12$) to a circular ($I_\bullet = \pi t^4/64$) shape.

The circular shape of the struts may be observed in the values of roundness ($R = (4\pi A_R)/(P^2)$) presented in Fig. 16 (b). Given the high roundness values (R = 0.89 to 0.93), the cross-sectional shape may be more usefully considered a circular geometry.
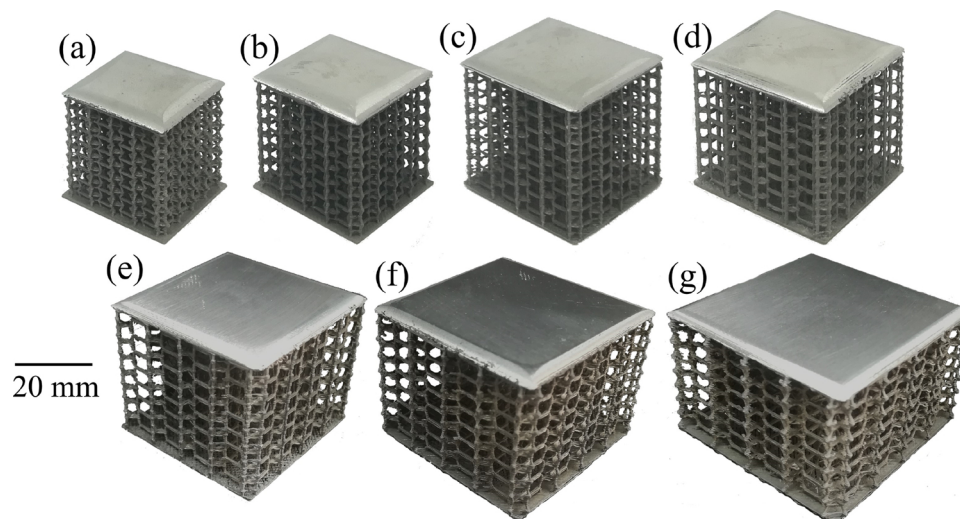
Fig. 8. Photographs of the cast Al lattices: (a) $\alpha = -30°$, (b) $\alpha = -20°$, (c) $\alpha = -10°$, (d) $\alpha = 0°$, (e) $\alpha = 10°$, (f) $\alpha = 20°$ and (g) $\alpha = 30°$.
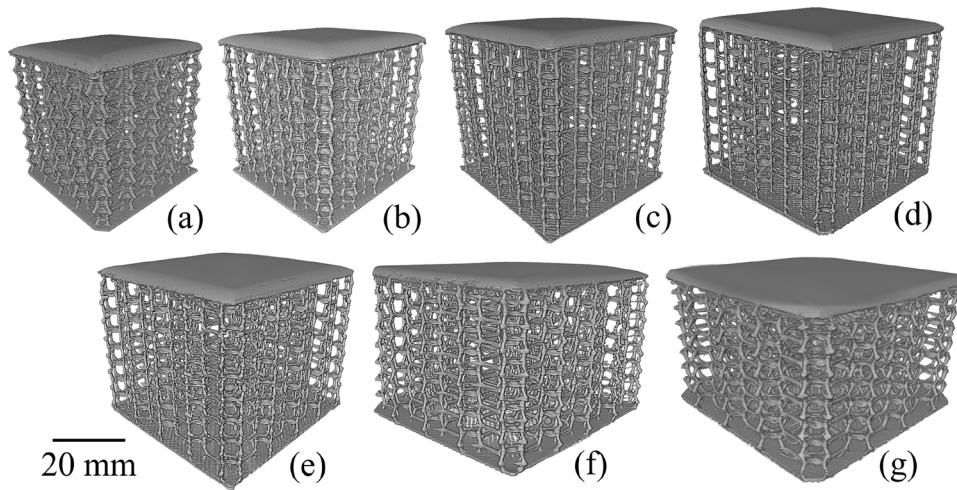
Fig. 9. μCT of the cast Al lattices: (a) α = -30˚, (b) α = -20˚, (c) α = -10˚, (d) α = 0˚, (e) α = 10˚, (f) α = 20˚ and (g) α = 30˚.
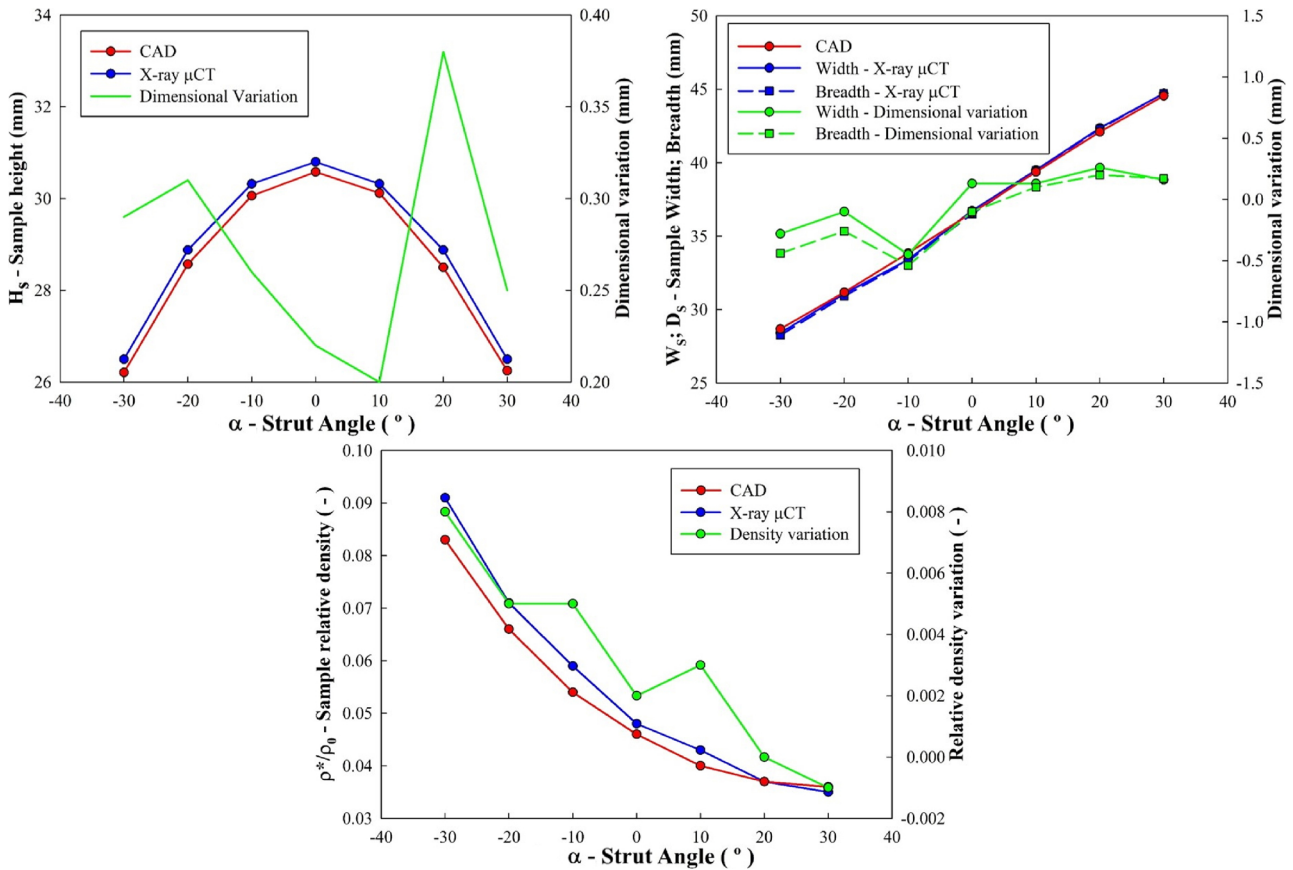

Fig. 10. Comparison between the dimensions of CAD and cast samples.

4. Conclusions

This study describes a novel route for producing low-cost periodic cellular lattices by an additive manufacturing assisted investment casting technique. The following conclusions can be drawn:

1. Optimization of the fabrication parameters (nozzle diameter and layer height) was essential to produce fine struts in the low specific density PLA investment models needed to fabricate ceramic casting molds. Using a 0.4 mm nozzle, struts as fine as 0.6 mm in cross-section could be produced.

2. 3D μCT measurements have shown that linear dimensions, such as horizontal rib and oblique strut lengths, may deviate from the CAD models. The final dimensions were up to 10 % greater than original CAD dimensions, and these deviations were more pronounced as rib and strut angles increased.

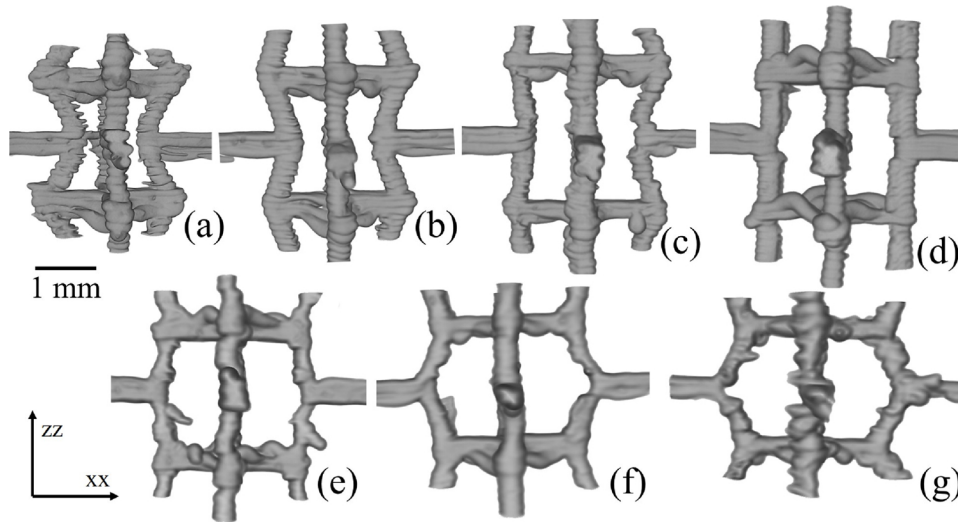3. The struts of cast samples presented an essentially circular shape.

Fig. 11. µCT of individual Al cells: (a) α = -30°, (b) α = -20°, (c) α = -10°, (d) α = 0°, (e) α = 10°, (f) α = 20° and (g) α = 30° samples (Build direction in ZZ axis).
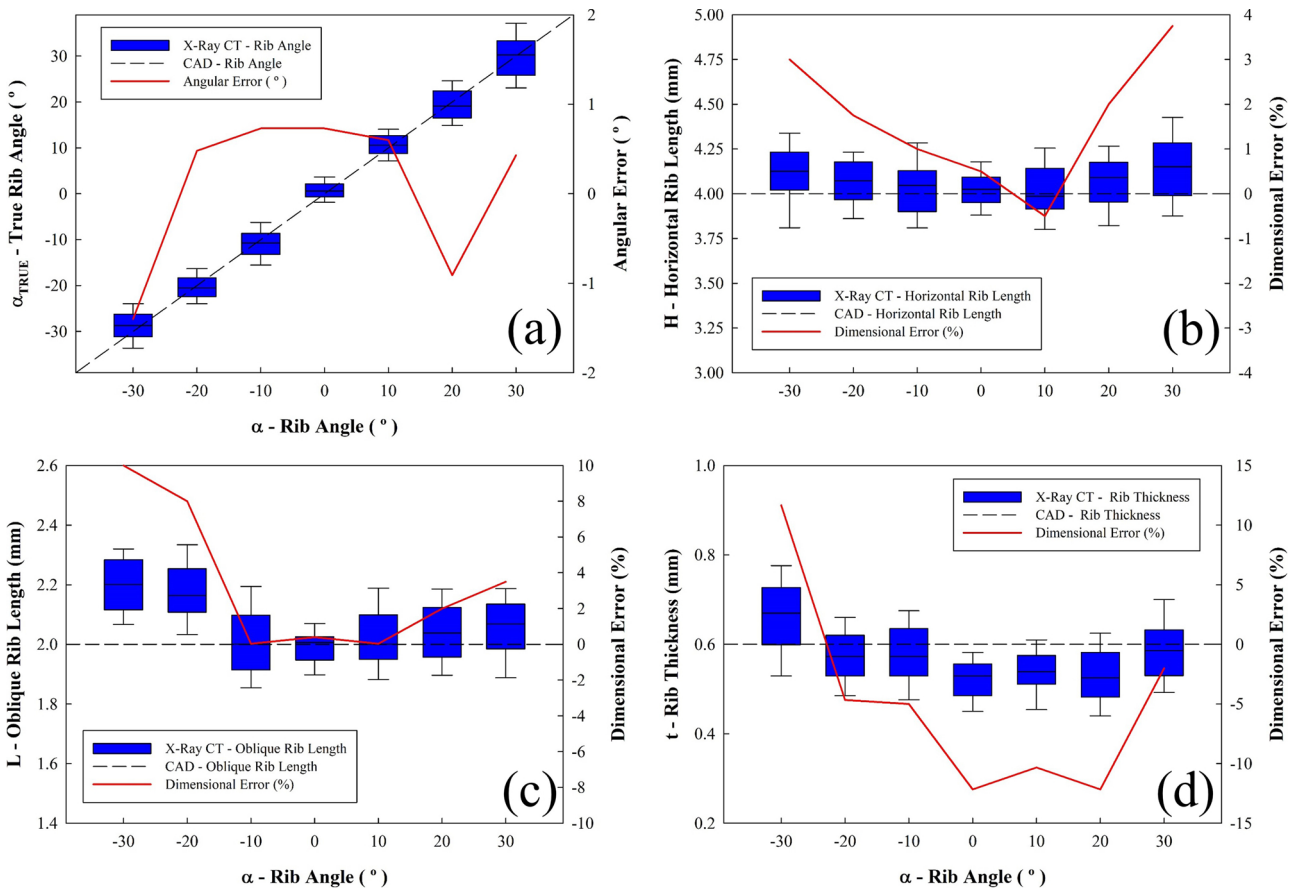

Fig. 12. Dimensional measurements from the µCT comparing CAD model dimensions: (a) strut angle (α), (b) horizontal rib length (h), (c) oblique strut length (l) and (d) rib and strut thickness (t).

The process was unable to produce square cross-sections as defined in the CAD model, due to the shape of the extrusion nozzle. Additionally, the final strut thickness of manufactured samples was lower than specified in CAD models, especially when the strut angle approximated zero (*i.e.* square honeycombs). These deviations affected the strut cross-sectional area and moment of inertia. Given that the main deformation mechanism of this kind of composites is strut flexure/buckling, this shape and any dimensional variations are likely to adversely impact their structural strength.

4. These dimensional deviations and defects originated in the 3D-printing of the polymer pattern. These could be minimized if the PLA investment model was fabricated using equipment with improved tolerance and enhanced extrusion control.

5. Despite the small dimensional and shape deviations, the described method is a promising route to produce fine metallic cellular lattices to high dimensional tolerances without the anisotropies

Table 4

Statistical significance of the strut dimensions to those prescribed by the CAD template.

α	-30	-20	-10	0	10	20	30
-30	■	●●	●●	●●	●●	●●	●●
-20		■	●●	●●	●●	●●	●●
-10			■	●●	●●	●●	●●
0				■	●	●●	●●
10					■	●●	●●
20						■	●●
30							■

H	-30	-20	-10	0	10	20	30
-30	■	●●	●●	●●	●●		
-20		■					●●
-10			■				●●
0				■			●●
10					■		●●
20						■	●
30							■

L	-30	-20	-10	0	10	20	30
-30	■	●●	●●	●●	●●		
-20		■					●●
-10			■				●●
0				■			●●
10					■		●●
20						■	●
30							■

t	-30	-20	-10	0	10	20	30
-30	■	●●	●●	●●	●●	●●	●●
-20		■		●●	●●	●●	
-10			■	●●	●●	●●	
0				■			●●
10					■		●●
20						■	●●
30							■

🟩 No significant difference.	●	p<0.05
🟥 Significant difference	●●	p<0.01
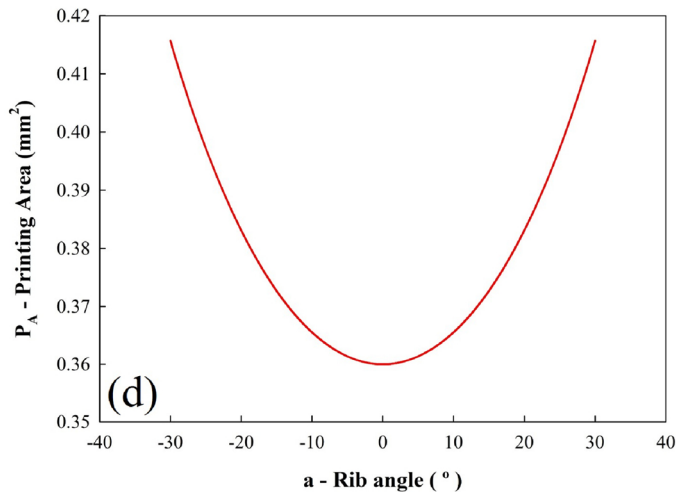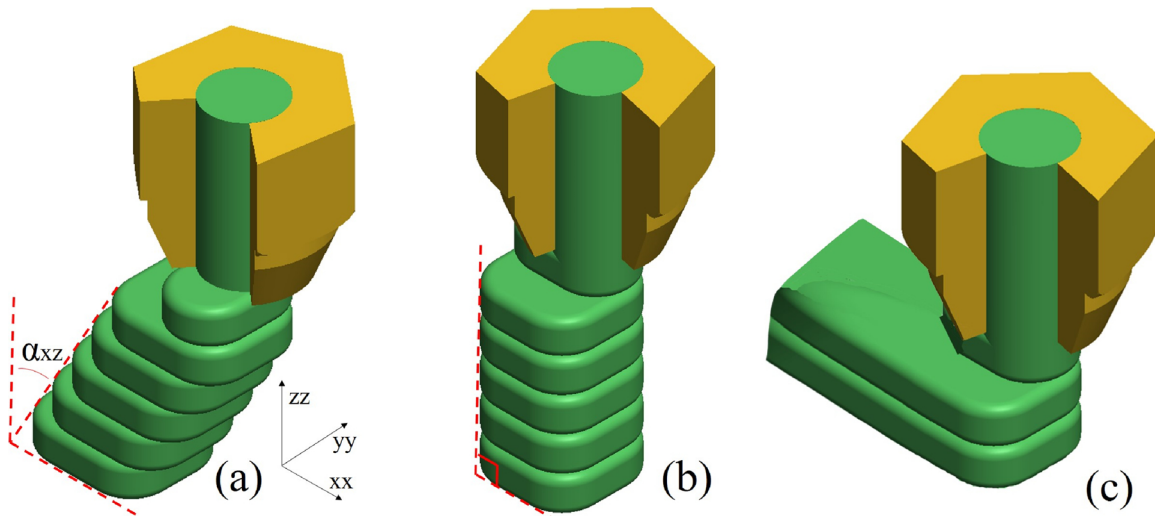
Fig. 13. Influence of angle on the printing area during the fused filament fabrication process: (a) oblique (α = 30°) struts, (b) vertical (α = 0°) struts and (c) horizontal ribs. (d) Printing area plot of for struts (t = 0.6 mm).
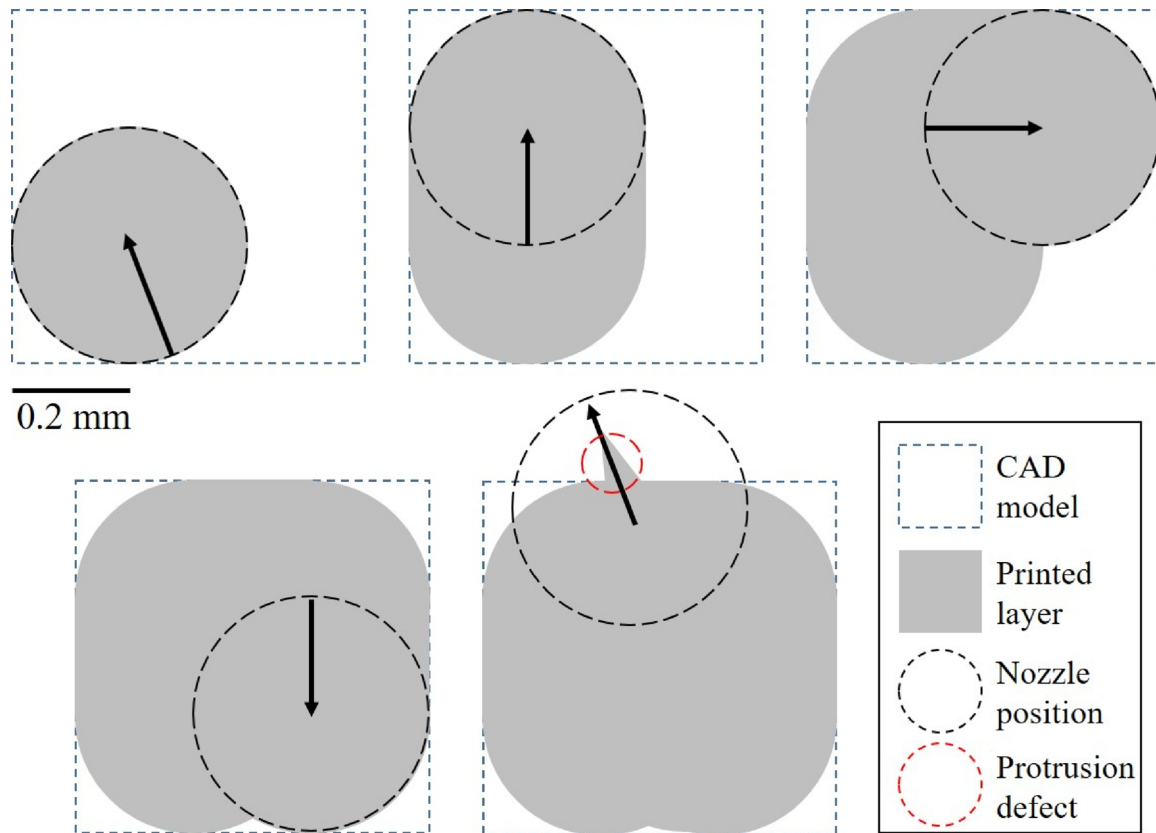
Fig. 14. Schematic illustrating the deviation in printed oblique strut cross-section from the CAD model (plan view).
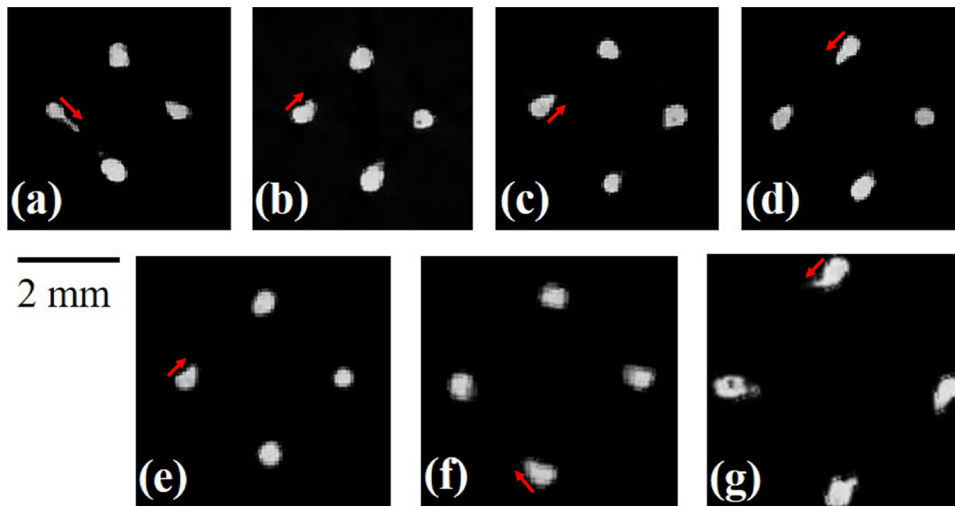

Fig. 15. Cross-sectional view through the reconstructed µCT volumes, showing detail for struts: (a) α = -30°, (b) α = -20°, (c) α = -10°, (d) α = 0°, (e) α = 10°, (f) α = 20° and (g) α = 30°. (Red arrows indicate protrusion defects) (For interpretation of the references to colour in this figure legend, the reader is referred to the web version of this article).

associated with conventional AM routes. Consequently it is a promising low-cost alternative for lattice manufacture compared to other AM techniques (*e.g.* SLM or EBM).

CRediT authorship contribution statement

V.H. Carneiro: Conceptualization, Investigation, Formal analysis. **S.D. Rawson:** Data curation, Writing - original draft, Writing - review & editing. **H. Puga:** Methodology, Resources, Writing - original draft, Writing - review & editing. **J. Meireles:** Validation, Supervision, Funding acquisition. **P.J. Withers:** Resources, Writing - original draft, Supervision, Writing - review & editing, Funding acquisition.

Declaration of Competing Interest

• All authors have participated in (a) conception and design, or analysis and interpretation of the data; (b) drafting the article or revising it critically for important intellectual content; and (c) approval of the final version.
• This manuscript has not been submitted to, nor is under review at, another journal or other publishing venue.
• The authors have no affiliation with any organization with a direct or indirect financial interest in the subject matter discussed in the manuscript
• The following authors have affiliations with organizations with direct or indirect financial interest in the subject matter discussed in the manuscript
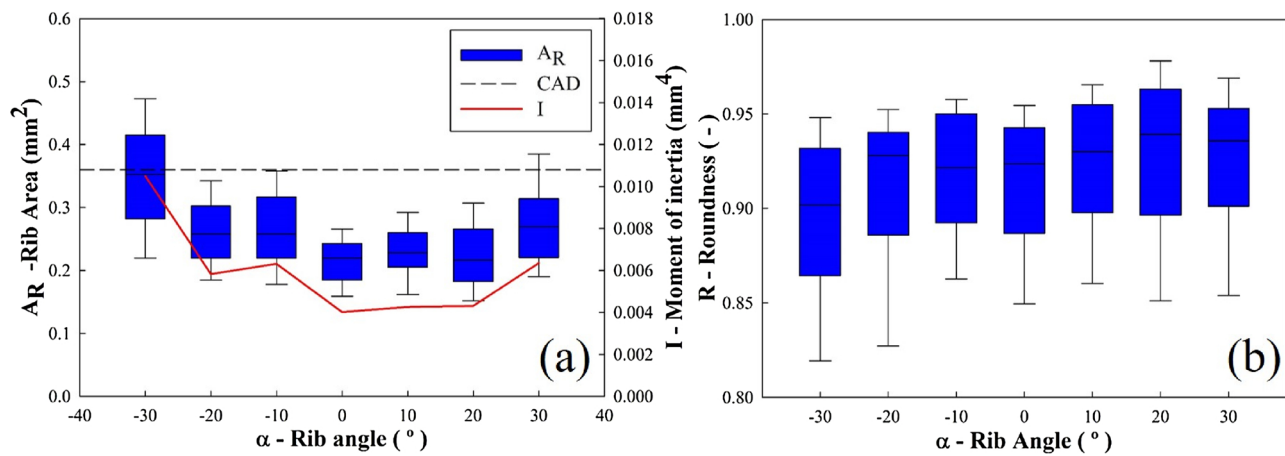
Fig. 16. Strut cross-section: (a) strut area and moment of inertia; (b) strut roundness (R = 1, means perfect circle).

Acknowledgements

Appendix A. Supplementary data

Supplementary material related to this article can be found, in the online version, at doi:https://doi.org/10.1016/j.addma.2020.101085.

References

[1] L.J. Gibson, M.F. Ashby, Cellular Solids: Structure and Properties, Cambridge university press, Cambridge, 1999.
[2] M.F. Ashby, T. Evans, N.A. Fleck, J. Hutchinson, H. Wadley, L. Gibson, Metal Foams: a Design Guide, Elsevier, Woburn, 2000.
[3] K.K. Sairajan, G.S. Aglietti, K.M. Mani, A review of multifunctional structure technology for aerospace applications, Acta Astronaut. 120 (2016) 30–42.
[4] L. Marsavina, Fracture mechanics of cellular solids, in: H. Altenbach, A. Öchsner (Eds.), Cell. Porous Mater. Struct. Process, Springer Vienna, Vienna, 2010, pp. 1–46.
[5] C. Meola, S. Boccardi, G. maria Carlomagno, Chapter 1 - composite materials in the aeronautical industry, in: C. Meola, S. Boccardi, G. maria Carlomagno (Eds.), Infrared Thermogr. Eval. Aerosp. Compos. Mater. Woodhead Publishing, 2017, pp. 1–24.
[6] H. Heo, J. Ju, D.-M. Kim, Compliant cellular structures: application to a passive morphing airfoil, Compos. Struct. 106 (2013) 560–569.
[7] L. Su, H. Liu, G. Yao, J. Zhang, Experimental study on the closed-cell aluminum foam shock absorption layer of a high-speed railway tunnel, Soil Dyn. Earthq. Eng. 119 (2019) 331–345.
[8] H. Mozafari, S. Khatami, H. Molatefi, Out of plane crushing and local stiffness determination of proposed foam filled sandwich panel for Korean Tilting Train eXpress – numerical study, Lightweight Mater. Struct. Solut. Transp. Appl. 66 (2015) 400–411.
[9] S. Yao, X. Xiao, P. Xu, Q. Qu, Q. Che, The impact performance of honeycomb-filled structures under eccentric loading for subway vehicles, Thin-Walled Struct. 123 (2018) 360–370.
[10] G. Chen, P. Zhang, J. Liu, Y. Cheng, H. Wang, Experimental and numerical analyses on the dynamic response of aluminum foam core sandwich panels subjected to localized air blast loading, Mar. Struct. 65 (2019) 343–361.
[11] V. Crupi, G. Epasto, E. Guglielmino, Comparison of aluminium sandwiches for lightweight ship structures: honeycomb vs. Foam, Mar. Struct. 30 (2013) 74–96.
[12] X. Zhang, L. Wei, Processing and damping capacity of NiTi foams with laminated pore architecture, J. Mech. Behav. Biomed. Mater. 96 (2019) 108–117.
[13] K. Hong, H. Park, Y. Kim, M. Knapek, P. Minárik, K. Máthis, A. Yamamoto, H. Choe, Mechanical and biocorrosive properties of magnesium-aluminum alloy scaffold for biomedical applications, J. Mech. Behav. Biomed. Mater. 98 (2019) 213–224.
[14] V.H. Carneiro, H. Puga, Deformation behaviour of self-expanding magnesium stents based on auxetic chiral lattices, Ciênc. Tecnol. Mater. 28 (2016) 14–18.
[15] J. Banhart, Light-metal foams—history of innovation and technological challenges, Adv. Eng. Mater. 15 (2013) 82–111.
[16] J. Banhart, Manufacture, characterisation and application of cellular metals and metal foams, Prog. Mater. Sci. 46 (2001) 559–632.
[17] V.H. Carneiro, H. Puga, J. Meireles, Positive, zero and negative Poisson's ratio non-stochastic metallic cellular solids: dependence between static and dynamic mechanical properties, Compos. Struct. 226 (2019) 111239.
[18] N. Wang, E. Maire, X. Chen, J. Adrien, Y. Li, Y. Amani, L. Hu, Y. Cheng, Compressive performance and deformation mechanism of the dynamic gas injection aluminum foams, Mater. Charact. 147 (2019) 11–20.
[19] K. Heim, F. García-Moreno, J. Banhart, Particle size and fraction required to stabilise aluminium alloy foams created by gas injection, Scr. Mater. 153 (2018) 54–58.
[20] D.K. Rajak, N.N. Mahajan, S. Das, Fabrication and investigation of influence of CaCO3 as foaming agent on Al-SiCp foam, Mater. Manuf. Process. 34 (2019) 379–384.
[21] H. Jain, G. Gupta, R. Kumar, D.P. Mondal, Microstructure and compressive deformation behavior of SS foam made through evaporation of urea as space holder, Mater. Chem. Phys. 223 (2019) 737–744.
[22] M. Vesenjak, M.A. Sulong, L. Krstulović-Opara, M. Borovinšek, V. Mathier, T. Fiedler, Dynamic compression of aluminium foam derived from infiltration casting of salt dough, Mech. Mater. 93 (2016) 96–108.
[23] H. Puga, V.H. Carneiro, C. Jesus, J. Pereira, V. Lopes, Influence of particle diameter in mechanical performance of Al expanded clay syntactic foams, Compos. Struct. 184 (2018) 698–703.
[24] O. Andersen, H. Göhler, C. Kostmann, P. Quadbeck, F. Diologent, D. Colas, B. Kieback, Powder metallurgically manufactured cellular metals from carat gold alloys for decorative applications, Met. Powder Rep. 73 (2018) 72–79.
[25] Y. Ma, X. Yang, C. He, K. Yang, J. Xu, J. Sha, C. Shi, J. Li, N. Zhao, Fabrication of in-situ grown carbon nanotubes reinforced aluminum alloy matrix composite foams based on powder metallurgy method, Mater. Lett. 233 (2018) 351–354.
[26] K.-J. Kang, Wire-woven cellular metals: the present and future, Prog. Mater. Sci. 69 (2015) 213–307.
[27] M.-G. Lee, G.-D. Ko, J. Song, K.-J. Kang, Compressive characteristics of a wire-woven cellular metal, Mater. Sci. Eng. A 539 (2012) 185–193.
[28] J. Hu, Q. Du, J. Gao, J. Kang, B. Guo, Compressive mechanical behavior of multiple wire metal rubber, Mater. Des. 140 (2018) 231–240.
[29] I.J. Gibson, Ashby Michael Farries, The mechanics of three-dimensional cellular materials, Proc. R. Soc. Lond. Math. Phys. Sci. 382 (1982) 43–59.
[30] N. Cohen, R.M. McMeeking, M.R. Begley, Modeling the non-linear elastic response of periodic lattice materials, Mech. Mater. 129 (2019) 159–168.
[31] H. Gu, S. Li, M. Pavier, M.M. Attallah, C. Paraskevoulakos, A. Shterenlikht, Fracture of three-dimensional lattices manufactured by selective laser melting, Int. J. Solids Struct. 180-181 (2019) 147–159.
[32] F. Rosa, S. Manzoni, R. Casati, Damping behavior of 316L lattice structures produced by Selective Laser Melting, Mater. Des. 160 (2018) 1010–1018.
[33] V. Crupi, E. Kara, G. Epasto, E. Guglielmino, H. Aykul, Static behavior of lattice structures produced via direct metal laser sintering technology, Mater. Des. 135 (2017) 246–256.
[34] S. Milles, B. Voisiat, M. Nitschke, A.F. Lasagni, Influence of roughness achieved by periodic structures on the wettability of aluminum using direct laser writing and direct laser interference patterning technology, J. Mater. Process. Technol. 270 (2019) 142–151.
[35] A. Ataee, Y. Li, C. Wen, A comparative study on the nanoindentation behavior, wear resistance and in vitro biocompatibility of SLM manufactured CP–Ti and EBM manufactured Ti64 gyroid scaffolds, Acta Biomater. 97 (2019) 587–596.
[36] A. Carré, M. Museau, P.-T. Doutre, F. Vignat, A method to determine the

depowdered height in lattices manufactured by electron beam melting, J. Manuf. Process. 34 (2018) 1–6.

[37] E. Hernández-Nava, C.J. Smith, F. Derguti, S. Tammas-Williams, F. Leonard, P.J. Withers, I. Todd, R. Goodall, The effect of defects on the mechanical response of Ti-6Al-4V cubic lattice structures fabricated by electron beam melting, Acta Mater. 108 (2016) 279–292.

[38] A.G. Demir, Micro laser metal wire deposition for additive manufacturing of thin-walled structures, Opt. Lasers Eng. 100 (2018) 9–17.

[39] Y. Ibrahim, Z. Li, C.M. Davies, C. Maharaj, J.P. Dear, P.A. Hooper, Acoustic resonance testing of additive manufactured lattice structures, Addit. Manuf. 24 (2018) 566–576.

[40] D.J. McGregor, S. Tawfick, W.P. King, Automated metrology and geometric analysis of additively manufactured lattice structures, Addit. Manuf. 28 (2019) 535–545.

[41] C. Qiu, S. Yue, N.J.E. Adkins, M. Ward, H. Hassanin, P.D. Lee, P.J. Withers, M.M. Attallah, Influence of processing conditions on strut structure and compressive properties of cellular lattice structures fabricated by selective laser melting, Mater. Sci. Eng. A. 628 (2015) 188–197.

[42] A. Du Plessis, D.-P. Kouprianoff, I. Yadroitsava, I. Yadroitsev, Mechanical properties and in situ deformation imaging of microlattices manufactured by laser based powder bed fusion, Materials 11 (2018) 1663.

[43] B.M. West, N.E. Capps, J.S. Urban, J.D. Pribe, T.J. Hartwig, T.D. Lunn, B. Brown, D.A. Bristow, R.G. Landers, E.C. Kinzel, Modal analysis of metal additive manufactured parts, Manuf. Lett. 13 (2017) 30–33.

[44] Y. Kok, X.P. Tan, P. Wang, M.L.S. Nai, N.H. Loh, E. Liu, S.B. Tor, Anisotropy and heterogeneity of microstructure and mechanical properties in metal additive manufacturing: a critical review, Mater. Des. 139 (2018) 565–586.

[45] X. Li, W. Tan, Numerical investigation of effects of nucleation mechanisms on grain structure in metal additive manufacturing, Comput. Mater. Sci. 153 (2018) 159–169.

[46] D.-S. Shim, J.-Y. Seo, H.-S. Yoon, K.-Y. Lee, W.-J. Oh, Additive manufacturing of porous metals using laser melting of Ti6Al4V powder with a foaming agent, Mater. Res. Express 5 (2018) 86518.

[47] A.D. Dressler, E.W. Jost, J.C. Miers, D.G. Moore, C.C. Seepersad, B.L. Boyce, Heterogeneities dominate mechanical performance of additively manufactured metal lattice struts, Addit. Manuf. 28 (2019) 692–703.

[48] L.S. Santos, S.K. Gupta, H.A. Bruck, Simulation of buckling of internal features during selective laser sintering of metals, Addit. Manuf. 23 (2018) 235–245.

[49] D. Herzog, V. Seyda, E. Wycisk, C. Emmelmann, Additive manufacturing of metals, Acta Mater. 117 (2016) 371–392.

[50] O. Zinovieva, A. Zinoviev, V. Ploshikhin, Three-dimensional modeling of the microstructure evolution during metal additive manufacturing, Comput. Mater. Sci. 141 (2018) 207–220.

[51] V.H. Carneiro, H. Puga, J. Meireles, Heat treatment as a route to tailor the yield-damping properties in A356 alloys, Mater. Sci. Eng. A. 729 (2018) 1–8.

[52] V.H. Carneiro, H. Puga, Solution treatment enhances both static and damping properties of Al–Si–Mg alloys, Metall. Mater. Trans. A. 49 (2018) 5942–5945.

[53] H. Puga, V.H. Carneiro, J. Barbosa, D. Soares, Effect of grain and secondary phase morphologies in the mechanical and damping behavior of Al7075 alloys, Met.

Mater. Int. 22 (2016) 863–871.

[54] Y. Tang, W.K. Tan, J.Y.H. Fuh, H.T. Loh, Y.S. Wong, S.C.H. Thian, L. Lu, Micro-mould fabrication for a micro-gear via vacuum casting, Seventh Asia Pac. Conf. Mater. Process. 7th APCMP 2006 192–193 (2007) 334–339.

[55] Y. Xue, W. Wang, F. Han, Enhanced compressive mechanical properties of aluminum based auxetic lattice structures filled with polymers, Compos. Part B Eng. 171 (2019) 183–191.

[56] C. Yang, B. Li, M. Ren, H. Fu, Micro precision casting based on investment casting for micro structures with high aspect ratio, Trans. Nonferrous Met. Soc. China. 19 (2009) s521–s525.

[57] D. Snelling, C. Williams, A. Druschitz, Mechanical and Material Properties of Castings produced via 3d printed molds, Addit. Manuf. 27 (2019) 199–207.

[58] J. Schindelin, I. Arganda-Carreras, E. Frise, V. Kaynig, M. Longair, T. Pietzsch, S. Preibisch, C. Rueden, S. Saalfeld, B. Schmid, J.-Y. Tinevez, D.J. White, V. Hartenstein, K. Eliceiri, P. Tomancak, A. Cardona, Fiji: an open-source platform for biological-image analysis, Nat. Methods 9 (2012) 676.

[59] V. Nienhaus, K. Smith, D. Spiehl, E. Dörsam, Investigations on nozzle geometry in fused filament fabrication, Addit. Manuf. 28 (2019) 711–718.

[60] V.H. Carneiro, H. Puga, Axisymmetric auxetics, Compos. Struct. 204 (2018) 438–444.

[61] K. Kardel, H. Ghaednia, A.L. Carrano, D.B. Marghitu, Experimental and theoretical modeling of behavior of 3D-printed polymers under collision with a rigid rod, Addit. Manuf. 14 (2017) 87–94.

[62] H. Zhao, Y. He, J. Fu, J. Qiu, Inclined layer printing for fused deposition modeling without assisted supporting structure, Robot. Comput.-Integr. Manuf. 51 (2018) 1–13.

[63] S. Bakrani Balani, F. Chabert, V. Nassiet, A. Cantarel, Influence of printing parameters on the stability of deposited beads in fused filament fabrication of poly (lactic) acid, Addit. Manuf. 25 (2019) 112–121.

[64] W. Liu, H. Song, Z. Wang, J. Wang, C. Huang, Improving mechanical performance of fused deposition modeling lattice structures by a snap-fitting method, Mater. Des. 181 (2019) 108065.

[65] O. Cansizoglu, O. Harrysson, D. Cormier, H. West, T. Mahale, Properties of Ti–6Al–4V non-stochastic lattice structures fabricated via electron beam melting, Mater. Sci. Eng. A. 492 (2008) 468–474.

[66] M. Leary, M. Mazur, J. Elambasseril, M. McMillan, T. Chirent, Y. Sun, M. Qian, M. Easton, M. Brandt, Selective laser melting (SLM) of AlSi12Mg lattice structures, Mater. Des. 98 (2016) 344–357.

[67] M. Suard, G. Martin, P. Lhuissier, R. Dendievel, F. Vignat, J.-J. Blandin, F. Villeneuve, Mechanical equivalent diameter of single struts for the stiffness prediction of lattice structures produced by Electron beam Melting, Addit. Manuf. 8 (2015) 124–131.

[68] BCN3D Sigma – Printing Properties, (2019) (Accessed 24 August 2019), https://www.bcn3dtechnologies.com/en/3d-printer/bcn3d-sigma/.

[69] H. Xia, J. Lu, G. Tryggvason, A numerical study of the effect of viscoelastic stresses in fused filament fabrication, Comput. Methods Appl. Mech. Eng. 346 (2019) 242–259.